Dissociation dynamics of diatomic molecules in intense laser fields: A scheme for the selection of relevant adiabatic potential curves

M. Magrakvelidze, C. M. Aikens, and U. Thumm

Phys. Rev. A **86**, 023402 — Published 1 August 2012

DOI: 10.1103/PhysRevA.86.023402

Dissociation dynamics of diatomic molecules in intense laser fields: a scheme for the selection of relevant adiabatic potential curves

M. Magrakvelidze[1], C. M. Aikens[2], and U. Thumm[1]
[1] *J. R. Macdonald Laboratory, Department of Physics, Kansas State University, Manhattan, Kansas 66506-2604, USA*
[2] *Department of Chemistry, Kansas State University, Manhattan, Kansas 66506-0401, USA*
(Dated: July 5, 2012)

We investigated the nuclear dynamics of diatomic molecular ions in intense laser fields by analyzing their fragment kinetic energy release (KER) spectra as a function of the pump-probe delay τ. Within the Born-Oppenheimer (BO) approximation, we calculated *ab initio* adiabatic potential energy curves and their electric dipole-couplings, using the quantum chemistry code GAMESS. By comparing simulated KER spectra as a function of either τ or the vibrational quantum-beat frequency for the nuclear dynamics on both individual and dipole-coupled BO potential curves with measured spectra, we developed a scheme for identifying electronic states that are relevant for the dissociation dynamics. We applied this scheme to investigate the nuclear dynamics in O_2^+ ions that are produced by ionization of neutral O_2 molecules in an ultra-short infrared (IR) pump pulse and dissociate due to the dipole coupling of molecular potential curves in a delayed IR probe laser field.

PACS numbers: 31.10.+z, 31.50.-x, 33.20.Xx, 34.50.Gb

I. INTRODUCTION

The control, time-resolved observation, and analysis of the nuclear dynamics in small diatomic molecules have been made possible by significant advances in femtosecond laser technology [1, 2]. In particular, using ultrashort IR pulses with a carrier wavelength of 800 nm and pulse lengths between 7 fs and 20 fs, the nuclear dynamics in H_2 and D_2 molecular ions have been studied by analyzing the KER of the fragments produced by a second delayed laser pulse [3–7]. In comparison with heavier molecules, the vibrational nuclear motion in H_2^+ (and its isotopes) is simple as it primarily involves the two lowest adiabatic potential curves of the molecular ion. For H_2^+, the dissociative wavepacket emerges mainly on the repulsive $|2p\sigma_u>$ state, while a bound oscillating part of the wavepacket may remain in the electronic ground state $|1s\sigma_g>$. The extension of these investigations to heavier molecules is not straightforward, and the interpretation of experimental data is intricate due to the large number of molecular potential curves involved. By analyzing KER spectra from dissociated oxygen ions as a function of the time delay, we recently found that usually several intermediate electronic states of the molecular ion contribute to the same KER [3, 6, 7]. In references [3] and [7] the dynamics of N_2, O_2, and CO molecules in intense laser pulses was studied using the Coulomb explosion (CE) imaging technique. In comparison with classical and quantum mechanical simulations, transiently populated intermediate states for molecular ions in different charge states and associated dissociation pathways were identified. The occurrence of vibrational revivals in measured KER spectra was scrutinized in reference [6] and allowed the identification of relevant molecular potential curves.

The purpose of this work is to systematically combine and jointly evaluate the information contained in different characteristic signatures of measured KER spectra. By revealing different aspects of the oscillating and dissociating motion in heavy diatomic molecular ions, we attempt to identify a manageable number of *relevant* electronic states within a large set of possible BO electronic states that exist for each heavy diatomic molecule in each charge state. We start our investigation in Sec. II by employing the General Atomic and Molecular Electronic Structure System (GAMESS) quantum chemistry code [8] to calculate potential curves and dipole coupling strengths between adiabatic potential curves using the multi-configuration (MC) self-consistent field (SCF) method with correlation consistent (cc) polarized triple-ζ (pVTZ) basis set (MCSCF/cc-pVTZ) [9, 10].

Next, in Sec. III. A, we numerically solve the time-dependent Schrödinger equation (TDSE) for the evolution of a given initial vibrational wavepacket in the molecular ion on a given BO potential curve. In our quantum mechanical calculations, we neglect molecular rotation and model the initial state of the molecular ion by assuming instantaneous ionization of the neutral parent molecule in the pump pulse based on the Franck-Condon approximation [11]. Our calculations provide KER spectra as a function of the pump-probe delay that reveal the vibrational period and revival times of binding molecular potential curves. The vibrational period and revival times in a *given* electronic state serve as a first criterion for selecting relevant potential curves. This selection process starts by comparing simulated KER spectra that were obtained in separate calculations under the assumption that the nuclear motion in the molecular ion proceeds on a single electronic potential curve with measured KER spectra. This comparison involves the scrutiny of simulated and measured KER spectra as a function of time and frequency. For this purpose we derive internuclear-distance (R)-dependent power spectra [12–14] by Fourier transformation of the calculated

time-dependent nuclear probability density. The power spectra allow us to identify vibrational quantum-beat (QB) frequencies associated with the bound motion of the vibrationally excited molecular ion. This enables us to further scrutinize the relevance of any given binding electronic state of the molecular ion by comparing revival times [15], oscillation periods, and QB frequencies with measured values.

After comparing separate calculations performed for individual BO molecular potential curves with measured KER spectra, we select a small set (in this work two) of curves that agree best with the measured data. In a final separate calculation, we then investigate the dissociative dynamics of the molecule, including dipole couplings between the selected electronic states of the molecular ion in the electric field of the probe-laser pulse (Sec. III. B). As an example we present numerical results for the dissociation of O_2^+ molecules. In Sec. III. C we compare two alternative methods for deriving KER spectra in nuclear wave-function-propagation calculation. The effect of an added long probe pedestal is investigated in Sec. III. D. Section IV compares measured KER spectra for O_2^+ ions with simulated spectra for dipole-coupled potential curves. A brief summary and our conclusions follow in Sec. V. We use atomic units unless indicated otherwise and relate potential energies to the vibrational ground state of the neutral electronic ground state ($X^3\Sigma_g^-$).

II. CALCULATION OF ADIABATIC POTENTIAL CURVES

To describe molecules in an intense laser field accurately one needs to consider both the electronic and also the nuclear degrees of freedom. The Hamilton operator for the unperturbed diatomic molecular system includes the kinetic energies of the nuclei and electrons T_R and T_e, the interaction between the nuclei $V_{RR} = Z_1 Z_2/R$ and the electrons $V_{ee} = \sum_{(i<j)} r_{ij}^{-1}$, and the electron-nuclear interaction $V_{eR} = \sum_i \sum_k Z_k r_{ik}^{-1}$,

$$H = T_R + V_{RR} + T_e + V_{eR} + V_{ee}. \quad (1)$$

Z_1 and Z_2 are the nuclear charges, R is internuclear distance, r_{ij} the distance between two electrons with labels i and j, and r_{ik} the distance between the nuclei and electrons labeled k and i.

No exact solutions of the Schrödinger equation with Hamiltonian (1) are known. However, simplified solution can be obtained within the BO approximation where the total wave function (WF) is expanded in products of nuclear and electronic WFs. The BO approximation is based on the fact that electrons are several thousand times lighter than nuclei and thus can be assumed to follow the nuclear motion adiabatically. That means that the nuclear kinetic energy term T_R in Eq. (1) can be dropped and that V_{RR} becomes a constant and thus irrelevant for the electronic motion considered in this work. In the BO approximation the correlation between the electrons (V_{ee}) still remains a challenge for numerical calculations. To overcome this difficulty, the so called "Hartree-Fock" (HF) "self-consistent field" (SCF) method is used [16, 17] in order to include the effect of V_{ee} approximately by considering each electron subject to an effective potential that is derived from the averaged charge distribution of all other electrons.

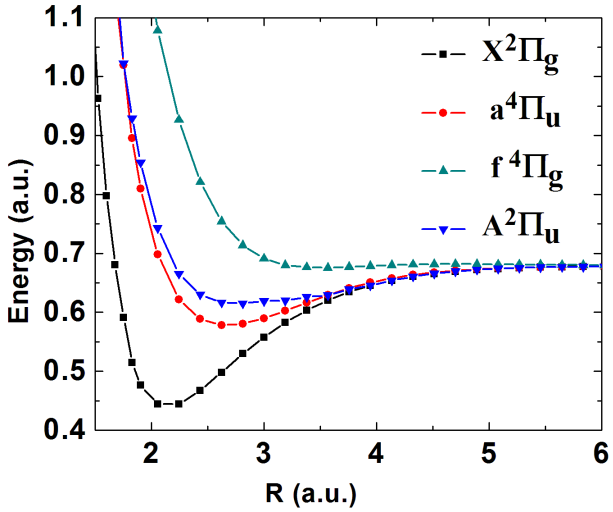

FIG. 1: (Color online) Potential energies for the O_2^+ molecular ion calculated using the MCSCF/cc-pVTZ method. The zero of the energy axis is taken as the $\nu = 0$ level of the $X^3\Sigma_g^-$ ground state of O_2.

For our calculations we used the multi configuration SCF (MCSCF) method, where a linear combination of configuration state functions (CSF), i.e. Slater determinants of molecular orbitals (MO), are employed to approximate the exact electronic WF of system. This is an improvement over the HF method where only one determinant is used. By variation of the set of coefficients in the MCSCF expansion in addition to the simultaneous variation of MO coefficients in the basis set expansion, the total electronic WF for a given BO channel is obtained with the lowest possible energy for a given set of occupied and active orbitals [16, 17]. We calculated potential curves and dipole-coupling strengths between adiabatic potential curves using the MCSCF/cc-pVTZ method (Detials are given in the Appendix.

A. Results

Figure 1 shows some of the calculated electronic states for the O_2^+ molecular ion. For selected states ($a^4\Pi_u$ and $f^4\Pi_g$ states), we compared data from the literature [18] with our MCSCF/cc-pVTZ results and found good agreement for both adiabatic potential curves and electric dipole transition matrix elements D_{ij} between two adiabatic electronic states that correspond to potential curves $V_i(R)$ and $V_j(R)$, where indices i and j label elec-

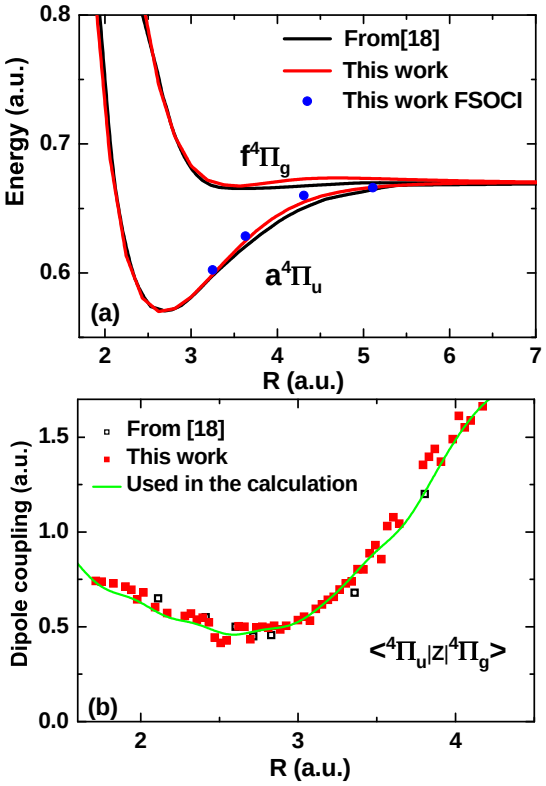

FIG. 2: (Color online) (a) Calculated potential energies and (b) dipole-coupling matrix elements from [18] using the MRD-CI/DZD method in comparison with our MCSCF/cc-pVTZ calculation. Blue dots in (a) correspond to the FSOCI /cc-pVTZ method.

tronic states. As an example, our calculated potential curves and dipole-coupling matrix elements for the $a^4\Pi_u$ and $f^4\Pi_g$ states of O_2^+ are compared to results in [18] in Figs. 2 (a) and (b) respectively. In Marian *et al.* [18], multi-reference double-excitation configuration interaction (MRD-CI) treatment [19] and a double-ζ basis set were used in the calculation (MRD-CI/DZP). MRD-CI includes electron correlation from excited determinants in addition to correlation within the active space.

For making sure that our MCSCF/cc-pVTZ method was sufficient compared to calculations that better represent electron correlation, we performed full second order CI calculations (FSOCI) for the $a^4\Pi_u$ state at four different internuclear distances. FSOCI calculations are similar to MRD-CI but include single and double excitations, while MRD-CI includes only double excitations. Blue dots in Fig. 2 (a) indicate results from FSOCI/cc-pVTZ calculations which are in good agreement (within 0.7%) with our MCSCF calculations (red line in Fig. 2 (a)). The computational time for FSOCI calculations is 3 orders of magnitude larger than for MCSCF calculations. Since the calculated values from both methods are similar, we used the numerically less expensive method (MCSCF) for obtaining electronic states and dipole-coupling matrix elements. Using a larger cc-pVTZ basis set than the basis used in [18], we can be confident that our calculated results are at least as accurate with regard to the complete basis set limit.

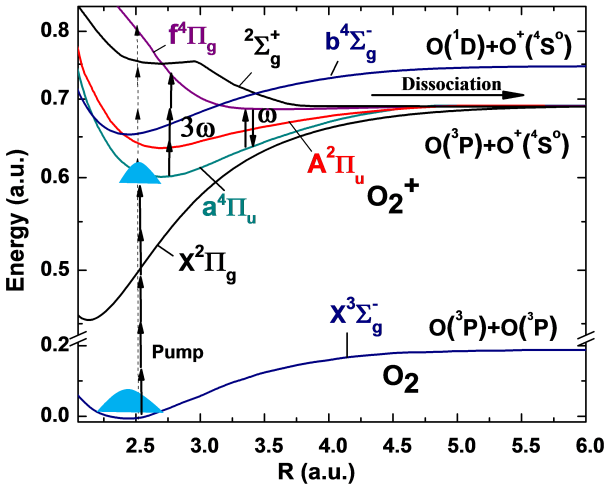

FIG. 3: (Color online) The nuclear dynamics in oxygen molecular ions. The pump-laser pulse launches a nuclear vibrational wavepacket onto O_2^+ potential curves (shown for $a^4\Pi_u$ and $f^4\Pi_g$ states) by ionizing O_2. After a variable time delay, an intense short probe pulse can cause the dissociation of the molecular ion through one-photon or net two-photon processes.

III. NUCLEAR DYNAMICS

A. Free nuclear motion in a single electronic state

The dynamics of the nuclear vibrational wavepacket can be reconstructed from the KER spectra obtained for a sequence of pump-probe delays τ. This is shown schematically in Fig. 3 for the $a^4\Pi_u$ and $f^4\Pi_g$ states where a pump pulse singly ionizes an oxygen molecule. In general, the pump pulse can ionize oxygen molecules to any state of O_2^+, for example $X^2\Pi_u$ and $b^4\Sigma_g^-$ states, but as our calculations show, several characteristic parameters, such as oscillation period, revival time, and QB frequency for the $a^4\Pi_u$ state match the experimental data best. The probe pulse is assumed to be linearly polarized along the molecular axis throughout this work. The excited oxygen molecule can dissociate through a one-photon or net two-photon process.

In order to reveal relevant intermediate electronic states of the molecular ion, we compared oscillation period and revival times of the bound motion of the wavepacket in a given electronic state with *measured* values. We also checked whether transitions between these states are dipole allowed and calculated the strength of

their dipole coupling in the electric field.

To identify which of the states are main contributors in the dynamics, we allowed the wavepacket to freely propagate on individual adiabatic potential curves $V_i(R)$ of the molecular ion. Neglecting molecular rotation, we solved the 1-D TDSE

$$i\frac{\partial}{\partial t}\Psi_i = [T_R + V_i(R)]\Psi_i \tag{2}$$

where the V_i are adiabatic potential curves.

Starting with neutral O_2 molecules in the ground state, we modeled the creation of the O_2^+ vibrational wavepacket by the pump pulse in Frank-Condon approximation [11, 12]. We solved (2) for the initial wavepacket

$$\Psi_i(R, t=0) = \sum_\nu a_{i,\nu}\phi_{i,\nu}(R). \tag{3}$$

that is expressed in terms of the Franck-Condon amplitudes $a_{i\nu}$. The indices ν correspond to vibrational states $\phi_{i,\nu}$ in the i'th bonding adiabatic electronic state of the molecular ion with vibrational energy $\omega_{i,\nu}$.

By either calculating the spectrum $\omega_{i,\nu}$ by diagonalization of the single-curve Hamiltonian $T_R + V_i(R)$ or by numerical wavepacket propagation of (2) subject to the initial condition (3), we obtained the evolution of (3) without external laser fields,

$$\Psi_i(R,t) = \sum_\nu a_{i,\nu}\phi_{i,\nu}(R)\ e^{-i\omega_{i,\nu}t}. \tag{4}$$

Repeating single-curve calculations for several potential energy curves, we aimed at identifying relevant electronic states by comparing characteristics of the bound wavepacket motion in $V_i(R)$, such as vibrational periods T_i and full and partial revival times $T_{rev,i}$ [15], that we obtained from probability density spectra (Fig. 4 (a,c)), with pump-probe-delay-dependent measured KER data [3, 6, 7, 12–14, 20, 21].

We obtained additional information for selecting electronic states that participate in the bound and dissociative nuclear motion of the molecular ion by comparing probability densities obtained from single-curve calculations with measured KER spectra as a function of the pump-probe delay (propagation time) and QB frequency [12–14]. By splitting the nuclear probability density

$$\begin{aligned}\rho_i(R,t) &= |\Psi_i(R,t)|^2 \\ &= \rho_i^{incoh}(R) \\ &+ \sum_{(\nu\neq\mu)} a^*_{i,\nu}a_{i,\mu}\exp(-i\omega_{i;\mu,\nu}t)\phi^*_{i,\nu}\phi_{i,\mu}\end{aligned} \tag{5}$$

into the time-independent incoherent contribution

$$\rho_i^{incoh}(R,t) = \sum_\nu |a_{i,\nu}|^2|\phi_{i,\nu}(R)|^2 \tag{6}$$

and the time-dependent coherent contribution $\sum_{(\nu\neq\mu)} a^*_{i,\nu}a_{i,\mu}e^{-i\omega_{i;\mu,\nu}t}\phi^*_{i,\nu}\phi_{i,\mu}$, we exposed quantum beats with frequencies $\omega_{i;\nu,\mu} = \omega_{i,\nu} - \omega_{i,\mu}$ of vibrational-state contributions to the nuclear wavepacket in a given potential curve $V_i(R)$. Fourier transformation of the coherent contribution over the finite sampling time T of pump-probe delays yields

$$\begin{aligned}&\widetilde{\rho}_i(R,\omega;T) \\ &= \frac{1}{\sqrt{\pi}}\int_0^t dt(\rho_i(R,t) - \rho_i^{incoh}(R))e^{-i\omega t} \\ &= \sqrt{2\pi}\sum_{\mu\neq\nu} a^*_{i,\nu}a_{i,\mu}\phi^*_{i,\nu}(R)\phi_{i,\mu}(R)\delta_T(\omega_{i;\nu,\mu}-\omega)\end{aligned} \tag{7}$$

and the power spectrum

$$W_i(R,\omega) = |\widetilde{\rho}(R,\omega;T)|^2, \tag{8}$$

where $\delta_T(\Omega)=1/2\pi\int_0^T e^{(i\Omega t)}dt$. The frequency resolution in W_i increases with T. Typically, sampling times of the order of a few picoseconds are required to clearly resolve vibrational beat frequencies in the power spectrum of heavy diatomic molecular ions.

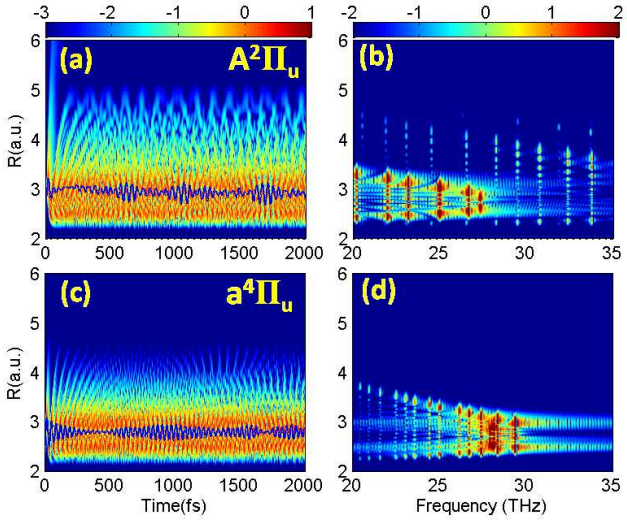

FIG. 4: (Color online) Single-curve calculations for the $A^2\Pi_u$ (a,b) and $a^4\Pi_u$ (c,d) states of O_2^+. Probability densities of the evolving vibrational wavepacket (a,c) and corresponding power spectra (b,d).

Examples for single-curve calculations are shown in Fig. 4 (a) and (b) for the $A^2\Pi_u$ and in Fig. 4 (c) and (d) for the $a^4\Pi_g$ states of O_2^+. The calculations were done with a numerical grid length of 310 (excluding the absorber lenght of 20) and a grid spacing 0.05 with time steps of $\Delta t = 1$. We also performed the same calculations for $X^2\Pi_u$ and $b^4\Sigma_g^-$ states of O_2^+ (Fig. 3, not shown in Fig. 4). Comparison of the simulated vibrational periods, revival times, and QB frequencies for a number of electronic states with measured KER spectra revealed the $a^4\Pi_u$ state as the best match to the experimental oscillation period and QB frequencies. Table I shows a comparison of the calculated and measured parameters

TABLE I: Comparison of calculated and measured revival times and ($\nu = 1 \rightarrow \nu = 2$) QB frequencies for four adiabatic electronic states of O_2^+.

	Calculation			Experimental values		
State	Oscill. period (fs)	Revival (fs)	QB freq. (THz)	Oscill. period (fs)	First full revival (fs)	QB freq. (THz)
$X^2\Pi_g$	17	670	58			
$a^4\Pi_u$	33	1000	30	34	$\backsim$1200	30
$A^2\Pi_u$	36	1100	28			
$b^4\Sigma_g^-$	29	900	35			

for each potential curve we tried in our calculations. The table reveals that closest to the experimental revival time of 1200 fs are the $a^4\Pi_u$ and $A^2\Pi_u$ states. However, the $A^2\Pi_u$ state can be ruled out because it generates QB frequencies that do not match the measured frequencies. Thus, the state $a^4\Pi_u$ appears to be the most relevant in the dissociative dynamics, which is also in agreement with the experimental findings in refs [7, 20].

B. Nuclear dynamics on dipole-coupled electronic states

Modeling the coherent motion of nuclear vibrational wavepackets on several Franck-Condon-populated adiabatic potential curves of the diatomic molecular ion, we allowed for dipole-coupling of (coherently launched) nuclear wavepackets $\Psi_i(R,t)$ in the electric field of the probe laser pulse by numerically propagating the coupled TDSE, using the split-operator Crank-Nicholson scheme,

$$i\frac{\partial}{\partial t}\begin{pmatrix}\Psi_1\\ \Psi_2\\ \vdots\end{pmatrix} = \begin{pmatrix}T_R+V_1 & D_{12} & \dots\\ D_{21} & T_R+V_2 & \dots\\ \dots & \dots & \ddots\end{pmatrix}\begin{pmatrix}\Psi_1\\ \Psi_2\\ \vdots\end{pmatrix}. \tag{9}$$

with the assumption that the wavepacket is launched from the ground state of O_2 to V_1 state of O_2^+ [12–14]. In analogy to (4-7), Fourier transformation of the total nuclear probability density

$$\rho(R,t) = \sum_i \rho_i(R,t) \tag{10}$$

for a finite sampling time T results in

$$\widetilde{\rho}(R,\omega;T) \sim \sum_i \widetilde{\rho_i}(R,\omega;T)$$
$$\sim \sum_i \sum_{\mu\neq\nu} a^*_{i,\nu}a_{i,\mu}\phi^*_{i,\nu}(R)\phi_{i,\mu}(R)\delta_T(\omega_{i;\nu,\mu}-\omega) \tag{11}$$

and the power spectrum

$$W(R,\omega) = |\widetilde{\rho}(R,\omega;T)|^2. \tag{12}$$

In order to simulate KER spectra, we numerically propagated the coupled equations (9) for a sufficiently long time, including field-free propagation of the nuclear wavepackets up to $\backsim$ 800 fs after the Gaussian-shaped 10 fs long probe pulse. This allowed us to separate the bound and dissociating parts of the nuclear motion by introducing the internuclear distance R_1 as an effective range for the bound nuclear motion. R_1 was determined such that the probability current associated with the dissociation of the molecular ion has relevant contributions for $R > R_1$, whereas bound motion remained restricted to distances $R < R_1$ (see Fig. (5)). Fourier transformation of the dissociating parts of the nuclear wavepackets over the interval $[R_1,\ R_{max}]$ yields the momentum representations of the dissociating wavepackets in the adiabatic channel i

$$\widetilde{\Psi}_i^{diss}(P,T) = \int_{R_1}^{R_{max}} dR\ \Psi_i^{diss}(R,T)e^{-iPR}, \tag{13}$$

where R_{max} is related to the size of the numerical grid, and R_1 is of the order of 4 in our applications below. By incoherently adding the corresponding momentum distributions $\rho_i^{incoh}(P,T) = |\Psi_i^{diss}(P,T)|^2$, we obtained the pump-probe-delay - dependent distribution of fragment KERs

$$C^{diss}(E,\tau) \propto \sum_i \rho_i^{incoh}(P,\tau), \tag{14}$$

where $E = P^2/2M$ is the kinetic energy per fragment with M being nuclear mass. Subtracting the large incoherent static contribution

$$C^{diss}_{incoh}(E) = \frac{1}{T}\int_0^T d\tau\ C^{diss}(E,\tau) \tag{15}$$

from C^{diss} we obtained the power spectrum as a function of the beat frequency $f = \omega/2\pi$

$$P^{diss}(E,f) = |\int_0^T d\tau\ C^{diss}_{coh}(E,\tau)e^{-i2\pi f\tau}|^2. \tag{16}$$

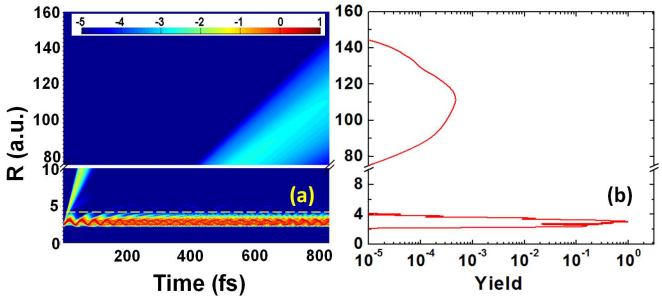

FIG. 5: (Color online) (a) Probability density $\rho(R,t)$ (Eq.10) for O_2^+ at fixed pump-probe delay $\tau = 10$ fs for the $a^4\Pi_u - f^4\Pi_g$ two-state calculation. The yellow dashed line corresponds $R_1 = 4$. The vibrational wavepacket is considered purely dissociative and propagated for 800 fs after the probe pulse. (b) Probability density as a function of internuclear distance R at $t = 800$ fs (logarithmic scale).

We refer to this method as "Fourier transformation (FT) method".

After conducting single-curve calculations for several potential curves of O_2^+ and identifying adiabatic electronic states, we solved the TDSE for the dipole coupled $a^4\Pi_u$ and $f^4\Pi_g$, $a^4\Pi_u$ and $^4\Sigma_g^+$, and $A^2\Pi_u$ and $^2\Sigma_g^+$ states in order to investigate the dissociation channels involved. The best match to the measured KER was obtained with the $a^4\Pi_u - f^4\Pi_g$ two-state calculation.

Figure 5 (a) shows the probability density (see equation (5) or (10)) as a function of propagation time and internuclear distance at a fixed pump-probe delay (τ = 10 fs) for a calculation with two coupled states, $a^4\Pi_u$ and $f^4\Pi_g$. In this calculation we assumed that initially only the $a^4\Pi_u$ state is populated, through a Franck-Condon transition from the ground state of O_2. Physically, this assumption can be justified by the fact that molecular ionization rates tend to be largest for states of the molecular ion that are energetically closest to the ground state of the neutral molecule. In our case this favors the initial population of the $X^2\Pi_g$ ground state of O_2^+. However, we also found that i) the vibrational period in the $X^2\Pi_g$ state is not at all seen in the experimental spectra and ii) due to the strongly binding nature of this state, it does not contribute to dissociation (for the range of laser parameters we considered). In contrast, the next higher lying bonding $a^4\Pi_u$ state of the molecular ion is shallow enough to strongly contribute to dissociation and therefore assumed to be the (by far) most relevant populated initial state. Also, we found that the KER spectra do not change if initially both $a^4\Pi_u$ and $f^4\Pi_g$ states are equally populated. The delayed probe pulse dipole couples the initial wavepacket motion with the $f^4\Pi_g$ state. As mentioned above, for the KER spectra calculations we took only the dissociative part of the wavepacket into account. The horizontal yellow dashed line indicates the internuclear separation R_1=4, beyond which the wavepacket is considered as purely dissociative. Figure 5 (b) shows the probability density on a logarithmic scale as a function of the internuclear distance 800 fs after the pump pulse.

We investigated the effect of the parameter R_1 on the KER spectra. The calculated KER, obtained using FT method, as a function of pump-probe delay is given in Fig. 6 for 10 fs, $3 \times 10^{14} W/cm^2$ probe pulses, and for R_1=3 (Fig. 6 (a)), R_1=4 (Fig. 6 (b)), R_1=4.5 (Fig. 6 (c)), and R_1=5 (Fig. 6 (d)). From Fig. 5 (b) one can see that for all values R_1>4.5 the KER spectra should give the same result. Indeed, the KER spectra shown in Fig. 6 (c) (R_1=4.5) and (d) (R_1=5), are almost the same. We found that simulations with R_1 = 4 yield the best agreement with measured KER spectra (in Sec. IV below).

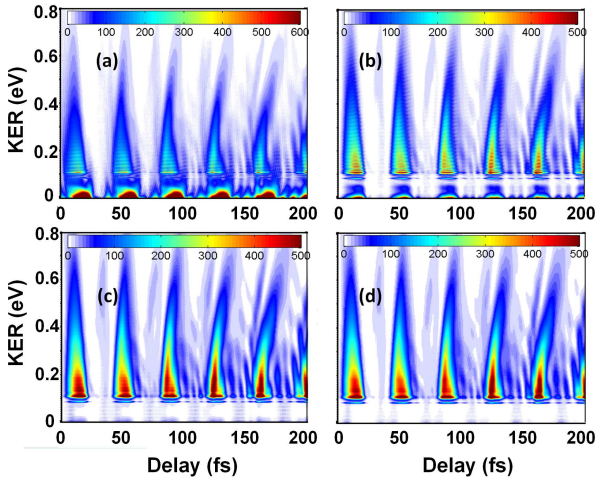

FIG. 6: (Color online) Calculated KER spectra for the dipole-coupled states $a^4\Pi_u$ and $f^4\Pi_g$ as a function of pump-probe delay for (a) R_1=3, (b) 4, (c) 4.5, and (d) 5 for a 10 fs, $3 \times 10^{14} W/cm^2$ probe laser pulse.

FIG. 7: Partitioning of the numerical grid into a propagation, virtual detector (VD), and absorption interval. The VD covers the interval $[R^{VD}_{min}, R^{VD}_{max}]$.

C. Comparison with the "virtual detector method" for simulating KER spectra

In addition to the FT calculations, we also applied an alternative, the so-called "virtual detector" (VD) method for obtaining KER spectra [22]. This method allows the computation of fragment-momentum distributions without propagating the wavepacket over a large numerical grid. In these VD calculations only, we used a grid length of R_{max}=40 with spacing ΔR = 0.01 (Fig. 7). The VD covers the R interval $[R^{VD}_{min}, R^{VD}_{max}]$=[6.5, 16.5]. The calculation was carried out for a total propagation time of 800 fs with time steps of Δt = 1. Applying the VD method, we calculated the momentum expectation value of the fragments, $p(t_i)$, at each time step t_i. We then combined fragment momenta that fall into small momentum bins in a histogram. From this histogram we obtained the KER spectrum (see [22] for more details).

The KER spectrum obtained with the VD method in Fig. 8 is almost identical with our results obtained using the FT method for R_1=4.5 (Fig. 6 (c))).

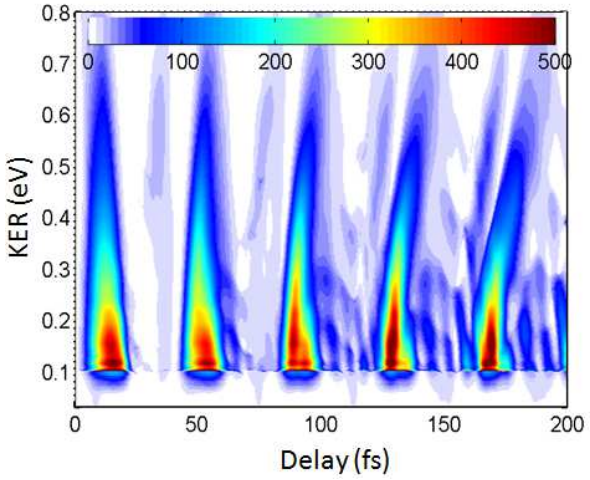

FIG. 8: (Color online) KER for dipole-coupled $a^4\Pi_u$ and $f^4\Pi_g$ states as a function of the pump-probe delay for calculations using the VD method [22] and a 10 fs, 3×10^{14} W/cm^2 probe laser pulse.

D. Influence of a probe-pulse pedestal

Figure 9 shows calculated KER spectra for the same laser parameters as in Fig. 8 using the FT method, with the exception that R_1=4 and a long Gaussian pedestal [12], with a length of 100 fs and intensity $5\times10^{11}W/cm^2$, is added to the main pulse (Fig. 10). Due to the long pedestal a prominent energy-dependent structure appears in the KER spectra. The reason why the energy-dependent structure is present only if a long pedestal is included can be explained based on the relation $\delta E \delta t \gtrsim h$. If only short pulses are present, the resolution in energy is such that one cannot observe the energy-dependent structure. On the other hand, if only the pedestal of the probe pulse is present, the oscillatory motion cannot be resolved [7]. For example, in order to resolve energies up to 0.1 eV, corresponding to the vibrational energy spacing in $a^4\Pi_u$, one needs to use pulses that are longer than 45 fs. The time-dependent structure is due to the periodic motion of the coherent vibrational wavepacket on the given O_2^+ state (the oscillation period for the $a^4\Pi_u$ state is 33 fs, Table I). A fragment-kinetic-energy dependent structure in the KER spectra was predicted as due to photoionization of vibrational states [7, 20].

IV. COMPARISON WITH EXPERIMENT

The calculated KER (14) as a function of the delay and the corresponding power spectrum (16) as a function of the QB frequency f for the $a^4\Pi_u - f^4\Pi_g$ two state calculation are shown in Fig. 11 (a) and (b) for a 10 fs probe pulse with a peak intensity of $3\times10^{14}W/cm^2$ and a 100 fs $5 \times 10^{11}W/cm^2$ Gaussian probe-pulse pedestal. Figures 11 (c) and (d) show the measured KER and power spec-

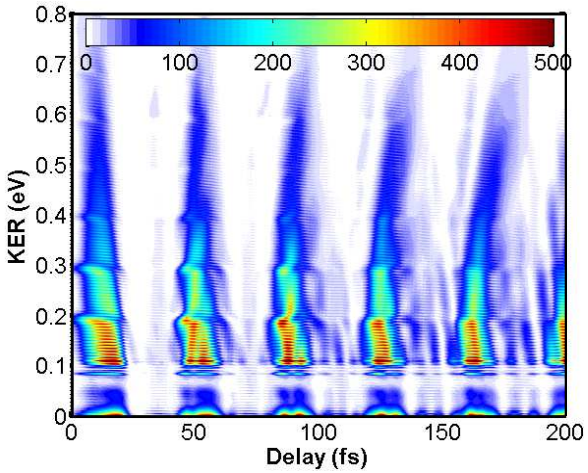

FIG. 9: (Color online) KER as a function of pump-probe delay for the calculations using the FT method described in Sec. III. B with $R_1 = 4$. The probe pulse includes the Gaussian pedestal. The parameters used for the main pulse were 10 fs, with intensity 3×10^{14} W/cm^2 and for the pedestal 100 fs with the intensity 5×10^{11} W/cm^2 (propagated for 800 fs after the end of FWHM of the probe).

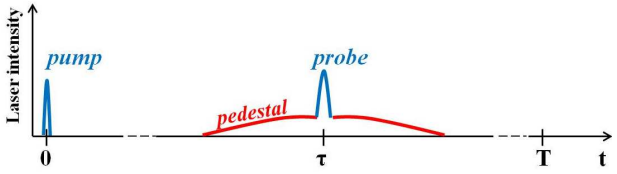

FIG. 10: (color online) Schematic of the temporal profile of pump and probe pulses.

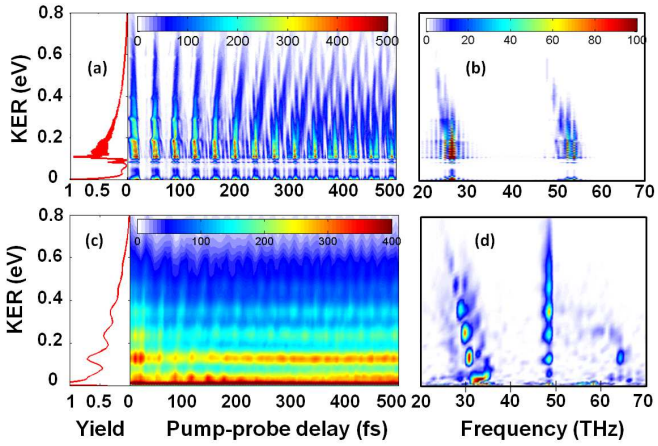

FIG. 11: (Color online) Calculated (a,b) and measured (c,d) [7] KER spectra for O_2^+ as a function of pump-probe delay (a,c) and frequency f (b,d). Calculated KER spectra include dipole-coupling of the $a^4\Pi_u$ and $f^4\Pi_g$ states by the 10 fs probe laser pulse with 3×10^{14} W/cm^2 peak intensity and a 100 fs 5×10^{11} W/cm^2 Gaussian pedestal. The power spectra (b,d) are obtained for a sampling time of 2 ps.

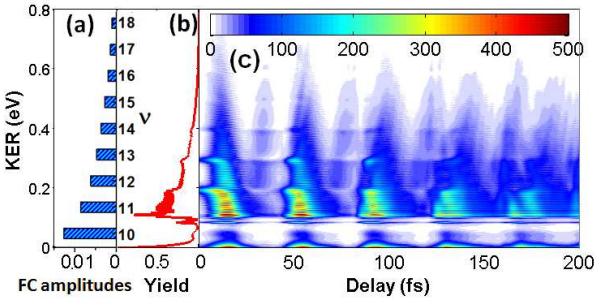

FIG. 12: (Color online) (a) Franck-Condon amplitudes $\{|a_\nu|^2\}$ for the vertical ionization from the ground state of O_2 to the $a^4\Pi_u$ state of O_2^+. (b) Delay-integrated focal-volume averaged KER as a function of the pump-probe delay, with main pulse length 10 fs, Gaussian pedestal length 100 fs, and for R_1=4. The focal-volume average is performed for peak intensities of the probe pulse between 10^{13} W/cm^2 and 4×10^{14} W/cm^2, with a fixed ratio of the peak intensities of the main pulse and pedestal of 0.01. (c) Delay-dependent focal-volume-averaged KER spectrum.

trum for a pump-probe intensity of 3×10^{14} W/cm^2 and a pulse duration of 10 fs. The sampling time in the experimental spectrum in Fig. 11 (d) is $T = 2000$ fs with the revival time 1200 fs (not shown) [7]. Comparison with the experimental results in Fig. 11 (c) and (d) shows that several features of the experimental data are reproduced. The oscillatory structure, with a period near 33 fs, is similar to the experimental period near 34 fs. The progressive tilt in the KER with increasing delay complies with a slightly larger return time of the more energetic spectral components of the vibrational wavepacket and was noticed earlier in the fragmentation of D_2^+ [4, 13, 14, 23] and O_2^+ [7]: a nuclear wavepacket with dominant spectral contribution from low-lying vibrational states oscillates faster than a vibrationally warmer wavepacket (corresponding to higher KER), causing the KER structure to tilt toward larger delays. The difference in the classical oscillation periods [13, 14] that correspond to wavepacket components centered around ν=11 and 13 vibrational states amounts to $\backsim$ 2.5 fs. This is consistent with the oscillation period difference between the peaks on energy cuts at 0.13 eV and 0.32 eV in the calculated KER spectra. However, the same difference in oscillation periods is obtained from the measured data for 0.14 eV and 0.25 eV.

For better comparison with the measured KER we focal-volume-averaged our calculations for the intensity range 10^{13} - 4×10^{14} W/cm^2 with steps of 10^{13} W/cm^2, keeping the ratio between the peak intensities of the main pulse and the pedestal constant, according to

$$\overline{C^{diss}}(E,\tau) = \frac{1}{N}\sum_{n=1}^{N} C^{diss}(I_n;E,\tau)$$

where C^{diss} is given by (14) (Fig. 12). The volume averaging effect on the energy-dependent structure is small. As in Figs. 9 and 11 (a), the energy-dependent structure, with a spacing of approximately 0.1 eV, is still seen in the focal volume averaged result (Fig. 12 (b)), where the separation between the peaks corresponds to the kinetic energies from the vibrational states in the $a^4\Pi_u$ electronic state: $\nu = 10$ (0.03 eV), $\nu = 11$ (0.13 eV), $\nu = 12$ (0.23 eV), $\nu = 13$ (0.32 eV), and $\nu = 14$ (0.41 eV). The expected KERs in the brackets are calculated as the dissociation energy limit of the $a^4\Pi_u$ state subtracted from the sum of the given vibrational level and photon energy. The vibrational state ν=10 of the $a^4\Pi_u$ state is energetically just above the dissociation limit of the $f^4\Pi_g - \omega$ field-dressed Floquet potential energy curve. Fig. 12 (a) shows the Franck-Condon amplitudes $\{|a_\nu|^2\}$ for vertical ionization. The population decreases as the vibrational quantum number increases. Thus, we conclude that the origin of the energy structure likely arises from the vibrational states as predicted in [7, 20].

V. SUMMARY

We developed a method for identifying the adiabatic electronic states involved in the dissociation of small molecules. We first calculated adiabatic potential curves and electric dipole-coupling matrix elements with the quantum chemistry code GAMESS. Next, we calculated nuclear probability-density spectra as a function of time and QB frequency for one molecular potential curve at a time and compared calculated revival times and beat frequencies with experimental data. After identifying relevant electronic states, we included laser-induced dipole-coupling in improved wavepacket propagation calculations and again compared resulting KER spectra with experimental data. We applied this scheme to O_2 molecules. After separately employing different combinations of electronic states of O_2^+ in our calculations, we concluded that the $a^4\Pi_u$ and $f^4\Pi_g$ states are key players in the dissociation dynamics, as the calculated and measured KER are similar with matching oscillation period and revival time (not shown in Fig.11).

Calculating KER spectra in nuclear wavepacket propagation calculations based on the Fourier-transformation method discussed in Sec. III. B and the virtual detector method in Sec. III. C, we obtained almost identical results. KER calculations including long probe-pulse pedestals were found to add an energy-dependent structure that is reminiscent of but does not clearly reproduce the energy dependence in measured KER spectra. The interpretation of this observed energy dependence remains a challenge for future investigations.

ACKNOWLEDGMENTS

We thank C. L. Cocke and I. Ben-Itzhak for valuable discussions and S. De for providing experimental data.

This work was supported by NSF grant PHY 1068752 and the Division of Chemical Sciences, Office of Basic Energy Sciences, Office of Science, U.S. DOE.

APPENDIX

A. Gaussian basis set

Atomic orbitals (AO) are modeled as Gaussian functions centered at each nuclei of the diatomic molecule (or molecular ion). These AO orbitals are linearly combined to form MOs with a set of expansion coefficients $\{C_i\}$. The MOs are multiplied with electron spin orbitals and combined to make Slater determinants in order to satisfy the Pauli exclusion principle. The CSF wavefunctions are equivalent to these Slater determinants (once the coefficients $\{C_i\}$ have been optimized). The CSF wavefunctions are linearly combined to create the MC wavefunction with coefficients $\{A_k\}$. The expansion coefficients $\{C_i\}$ and $\{A_k\}$ are determined simultaneously based on a variational principle [11].

The appropriate choice of basis functions is important for the accuracy of the calculated potential curves. The basis set is the set of (mathematical) functions (for example Gaussians) from which the WF is constructed. Since HF and MCSCF methods are variational, large basis sets lead to more accurate results. The basis set with two Gaussians on each AO is called a "double-ζ" basis. The higher the number of Gaussians used for each AO the more complete the basis is (multiple-ζ basis set). We used the Dunning-type correlation-consistent polarized valence triple-ζ basis set (cc-pVTZ) [24]. The "Dunning-type basis set" is an example of a multiple-ζ basis set. The "correlation-consistent" part of the name indicates that the basis set was optimized for calculations including electron correlation through excited CSFs.

B. Configuration state wavefunctions

The MCSCF WFs were optimized with the $[(1\sigma_g)^2(1\sigma_u)^2(2\sigma_g)^2(2\sigma_u)^2]$ "frozen core", meaning that the occupations of those MOs were not allowed to vary. The calculations were done for fixed internuclear separations R with steps of 0.02 Å. Dipole-coupling matrix elements for different R were calculated including configuration interaction within the graphical unitary group approach (GUGA) [25].

The ground state of the oxygen molecule has the configuration $[(1\sigma_g)^2(1\sigma_u)^2(2\sigma_g)^2(2\sigma_u)^2](3\sigma_g)^2(1\pi_u)^4(1\pi_g)^2$. A large number of final molecular ion states with different multiplicities and symmetries can be generated after valence photoionization. Those states are given in Table II. The table shows the main configurations that contribute more than 70% to the norm of the MC-SCF WF. GAMESS outputs only designate electronic configurations. To link the calculated potential curves and dipole-coupling matrix elements to a given MCSCF state, we used Table II.

TABLE II: Electronic configurations (molecular orbitals with occupancy) of the calculated MCSCF states of O_2^+

State	Main electronic configuration							
	$1\sigma_g$	$1\sigma_u$	$2\sigma_g$	$2\sigma_u$	$3\sigma_g$	$1\pi_u$	$1\pi_g$	$3\sigma_u$
$X^2\Pi_g$	2	2	2	2	2	4	1	0
$a^4\Pi_u$	2	2	2	2	2	3	2	0
$A^2\Pi_u$	2	2	2	2	2	3	2	0
$b^4\Sigma_g^-$	2	2	2	2	1	4	2	0
$f^4\Pi_g$	2	2	2	2	2	2	3	0
$^4\Sigma_g^+$	2	2	2	2	1	4	2	0

The MCSCF process minimizes energy using the variational principle."Root switching" can be a problem if two states are close in energy and MO and CSF coefficients are only optimized for one MCSCF state. To avoid this problem, we carried out state-averaged MCSCF calculations [26], where MO orbitals are optimized not for any one state energy E_j (which is usually the ground state), but for the average of two or more states $\overline{E} = \sum_j^N w_j E_j$, where N is the number of states (in our case 14) included in the average and the coefficients w_j are positive constants with normalization $\sum_j w_j = 1$. The MCSCF WFs are optimized to minimize the energies E_j. The number of MOs used in the variation space was 60; the number of the Cartesian Gaussian basis functions (atomic orbitals) used was 70. In MCSCF calculations, the specification of how many MO are occupied is crucial. One needs to specify the so called "active" space. MCSCF active space choices are often abbreviated as "(m,n)" where m is the number of active electrons and n is the number of orbitals. As an active space we used MCSCF (7, 6) for O_2^+. The six orbitals are the σ, π, σ^*, and π^* orbitals of O_2.

C. Geometry optimizations

When performing computations it is important to understand the geometry of the molecule, since many of the physical and chemical properties of the molecule depend on it. We optimized the molecular geometry of neutral (equilibrium internuclear distance 1.152Å) and singly charged (equilibrium internuclear distance 1.087Å) oxygen molecules using restricted open-shell SCF WFs, where the occupation of closed shells by the electrons are assumed to be fixed, with the WFs represented as a single Slater-determinant. "Restricted" indicates that the spin-up and spin-down orbital coefficients in the expansion and energies are the same. The symmetry used was D_{4h} for the linear molecule with inversion center [27], since the full $D_{\infty h}$ point group is not supported in GAMESS.

[1] A. H. Zewail, Science **242**, 1645 (1988).

[2] H. Niikura, D. M. Villeneuve, and P. B. Corkum, Phys. Rev. A **73**, 021402(R) (2006); J. H. Posthumus, Rep. Prog. Phys **67**, 623 (2004).

[3] I. A. Bocharova , A. S. Alnaser, U. Thumm, T. Niederhausen, D. Ray, C. L. Cocke, and I. V. Litvinyuk, Phys. Rev. A **83**, 013417 (2011).

[4] T. Ergler, A. Rudenko, B. Feuerstein, K. Zrost, C. D. Schr"oter, R. Moshammer, and J. Ullrich, Phys. Rev. Lett. **97**, 193001 (2006).

[5] A. S. Alnaser, B. Ulrich, X. M. Tong, I. V. Litvinyuk, C. M. Maharjan, P. Ranitovic, T. Osipov, R. Ali, S. Ghimire, Z.Chang, C. D. Lin, and C. L. Cocke, Phys. Rev. A **72**, 030702(R) (2005).

[6] S. De, I. A. Bocharova, M. Magrakvelidze, D. Ray, W. Cao, B. Bergues, U. Thumm, M. F. Kling, I. V. Litvinyuk, and C. L. Cocke, Phys. Rev. A **82**, 013408 (2010).

[7] S. De, M. Magrakvelidze, I. A. Bocharova, D. Ray, W. Cao, I. Znakovskaya, H. Li, Z. Wang, G. Laurent, U. Thumm, M. F. Kling, I. V. Litvinyuk, I. Ben-Itzhak, and C. L. Cocke, Phys. Rev. A **84**, 043410 (2011).

[8] M. S. Gordon and M. W. Schmidt "Advances in electronic structure theory: GAMESS a decade later". In: C. E. Dykstra, G. Frenking. K. S. Lim, and G. E. Scusaria. Theory and Applications of Computational Chemistry, the first 40 years. Elsevier, Amsterdam (2005).

[9] M. W. Schmidt and M. S. Gordon, Annu. Rev. Chem. Phys, **49**, 233 (1998).

[10] C. J. Cramer, "Essentials of Computational Chemistry Theories and Models", John Wiley & Sons Ltd., Chichester, England, 2nd ed. (2004).

[11] B. H. Bransden, and C. J. Joachain, "Physics of Atoms and Molecules", 2nd ed., Prentice-Hall, New York (2003).

[12] U. Thumm, T. Niederhausen, and B. Feuerstein, Phys. Rev. A **77**, 063401 (2008); M. Magrakvelidze, F. He, T. Niederhausen, I. V. Litvinyuk, and U. Thumm, Phys. Rev. A **79**, 033410 (2009); M. Winter, R. Schmidt, and U. Thumm, New J. Phys. **12**, 023020 (2010).

[13] B. Feuerstein, Th. Ergler, A. Rudenko, K. Zrost, C. D. Schröter, R. Moshammer, J. Ullrich, T. Niederhausen, and U. Thumm, Phys. Rev. Lett. **99**, 153002 (2007);

[14] T. Niederhausen and U. Thumm, Phys. Rev. A **77**, 013407 (2008).

[15] R. W. Robinett, Physics Reports **392**, 1 (2004).

[16] D. R. Fock, Math. Proc. of the Cambridge Phil. Society **24**, 89 (1928).

[17] C. C. J. Roothaan, Rev. Mod. Phys. **23**, 69 (1951).

[18] C. M. Marian, R. Marian, S. D. Peyerimhoff, B. A. Hess, R. J. Buenker, and G. Seger, Molecular Physics **46** (4) 779 (1982).

[19] R. J. Buenker, and S. D. Peyerimhoff, "New Horizons of Quantum Chemistry", edited by P. O. Lowdin and B. Pullman, Reidel: Dordrecht (1983); p 183.

[20] M. Zohrabi, J. McKenna, B. Gaire, N. G. Johnson, K. D. Carnes, S. De,I. A. Bocharova, M. Magrakvelidze, D. Ray, I. V. Litvinyuk, C. L. Cocke, and I. Ben-Itzhak, Phys. Rev. A **83**, 053405 (2011); A. M. Sayler, P. Q. Wang, K. D. Carnes, B. D. Esry, and I. Ben-Itzhak, Phys. Rev. A **75**, 063420 (2007).

[21] M. Magrakvelidze, O. Herrwerth, Y. H. Jiang, A. Rudenko, M. Kurka, L. Foucar, K. U. Kühnel, M. Kübel, Nora G. Johnson, C. D. Schröter, S. Düsterer, R. Treusch, M. Lezius, I. Ben-Itzhak, R. Moshammer, J. Ullrich, M. F. Kling, and U. Thumm, submitted to Phys. Rev. A (2012).

[22] B. Feuerstein and U. Thumm, J. Phys. B **36**, 707 (2003).

[23] B. Feuerstein and U. Thumm, Phys. Rev. A **67**, 063408 (2003).

[24] T. H. Dunning, J. Chem. Phys. **90**, 1007 (1989).

[25] M. D. Gould and J. Paldus, J. Chem. Phys. **92** (12), 7394 (1990).

[26] R. N. Diffenderfert and D. R. Yarkony, J. Phys. Chem. **86** (26), 5098 (1982).

[27] F. A. Cotton, "Chemical applications of group theory", a Wiley-Iinterscience Publication, New York, 3rd ed. (1990).